Experiments in Fluids (2018) 59:177
https://doi.org/10.1007/s00348-018-2630-0

RESEARCH ARTICLE

High-speed velocimetry in microfluidic protein mixers using confocal fluorescence decay microscopy

Venkatesh Inguva[1] · **Jonathan P. Rothstein**[1] · **Osman Bilsel**[2] · **Blair J. Perot**[1]

Received: 14 June 2018 / Revised: 21 September 2018 / Accepted: 3 October 2018

Abstract

A method to measure fluid speeds on the order of 10,000 mm/s in microchannels is presented. A microfluidic protein mixer is manufactured with a 170 µm microscope coverslip bottom that interfaces with a confocal florescence microscope using a water-immersed Olympus *UPLSAPO 60XW* objective to create a diffraction-limited confocal volume. A diode laser with a repetition rate of 1 MHz is used to study Poiseuille flows at average speeds of 5000, 6000 and 7000 mm/s by exciting tris(2,2′-bipyridine)ruthenium(II) hexafluorophosphate solution at 1 µmol/L concentration flowing through the micro-mixer in the confocal volume. Decays collected using a time-correlated single photon counting card at each grid point are characterized by the first moment of the decay and curve fitted with the theoretical Poiseuille flow solutions. It was found that curve fitting with higher average speeds results in lower errors. A fluorescence correlation study was then carried out at different depths in the micro-mixer to understand the raw data profiles observed using the diode laser. A mixing study was then carried out using a Ti-Sapphire laser with a repetition rate of 3.8 MHz. A Poiseuille flow at 7000 mm/s was measured using the Ti-Sapphire laser and then curve fitted to the theoretical Poiseuille flow solution. The curve fit was then applied to the complicated flow region to determine speed. Results of the experimental mixing study are also compared to direct numerical simulation results.

Graphical abstract An experimental technique to measure speeds in the complicated mixing region of a protein mixer is developed. Results show that when flow is bounded asymmetrically between a rough wall and smooth wall, the flow shows affinity for the smooth wall during the mixing process. The Reynolds number for this is flow is 245 indicating flow in the transitional turbulence regime.

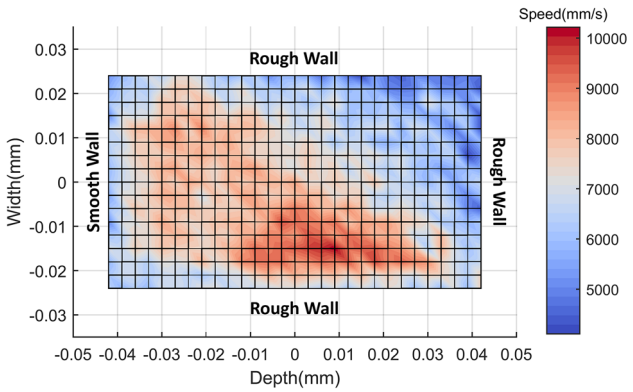

1 Introduction

Current state-of-the-art techniques to measure velocity in microchannels involve some form of micro particle image velocimetry (µPIV). µPIV differs from traditional particle image velocimetry in that the entire channel is illuminated

Electronic supplementary material The online version of this article (https://doi.org/10.1007/s00348-018-2630-0) contains supplementary material, which is available to authorized users.

✉ Venkatesh Inguva
vinguva@umass.edu

Extended author information available on the last page of the article

Published online: 09 November 2018

and the plane of measurement is defined by the depth-of-field of the recording lens (Williams et al. 2010). Numerous techniques exist to illuminate the observation volume and create different spatial resolutions for which particles can be tracked.

Evanescent wave μPIV (Zettner and Yoda 2003) uses illumination from the total internal reflection of the illumination source between the glass–water interface to measure velocity. Illumination occurs only 380 nm from the glass boundary making this technique ideal for near wall measurements (Williams et al. 2010). The in-plane spatial resolution was 40 μm and the speed of the observing camera was 30 Hz. The maximum speed this technique can measure is 1.2 mm/s. For near wall measurements, this limit on the maximum speed is more than adequate.

A high speed μPIV developed by Shinohara et al. (2004) used a typical μPIV system (Williams et al. 2010) but with a high speed camera of 2000 frames per second and a spatial resolution of 2.2 μm × 2.2 μm was used to determine the velocity in a flow of water and butyl acetate. The maximum speed this high-speed technique can measure is 4.4 mm/s.

A high-speed scanner for a confocal μPIV system with multiple micro-lenses and pinholes on a rotating disk was developed by Tanaami et al. (2002). The system illuminated the microfluidic channel with numerous laser beams allowing quick sampling of the velocity. Assuming the spatial resolution of the system is the full width at half maximum of the confocal volume which in this case is 0.6 μm and the time resolution is 1 frame/ms, the maximum speed this system can measure is 0.6 mm/s. Another high-speed confocal μPIV system (Kinoshita et al. 2007) has an in-plane spatial resolution of 9.1 μm × 9.1 μm with a camera frame rate of 2000 frames per second. The maximum speed this system can measure is 18.2 mm/s. However, confocal μPIV systems can only measure steady-state flow situations (Williams et al. 2010).

A review of microfluid mixers is presented by Kathuria et al. (2013). Turbulent microfluidic mixers developed by Matsumoto et al. (2007), Majumdar et al. (2005) and Gobby et al. (2001) typically operate at speeds of 7000–50,000 mm/s. Other groups led by Li and Olsen (2006) and Natrajan and Christensen (2009) also have used microscopic PIV to measure speeds on the order of 12,000 mm/s at resolutions of 14 μm by 14 μm using a CCD camera and have determined turbulence statistics from instantaneous velocity fields.

In this paper, we present a technique that does not use an imaging camera. This removes the upper limits on speed and velocity that the framerate of the camera imposes. Instead, fluorescence decays due to velocity are collected from a confocal fluorescence microscope interfaced to a time-correlated single photon counting (TCSPC) card are used to determine speed. Decay events lasting 30 ps (Van Oort et al. 2008) can be measured by the TCSPC card meaning the theoretical maximum speed this system can measure is upwards of a 1,000,000 mm/s. Like other confocal PIV measurement techniques, this approach measures time-averaged speeds at resolutions of 3 μm by 3 μm for 100 μm deep channels and possibly higher resolutions for shallower channels.

2 Methods

A confocal fluorescence microscope setup, as shown in Fig. 1, is used to collect a florescence decay signal which contain information about the speed of the fluid flowing through the diffraction-limited confocal volume by overfilling the objective using a beam expander. The period between pulses of the diode laser is 1000 ns (1 MHz repetition rate) to allow the system to measure speeds near the wall, but not at the wall, and at a wavelength of 450 nm. In principle, a slower repetition rate will allow measurements of speed closer to the wall where the speed is slower. The dye chosen to provide the fluorescence upon excitation is tris(2,2′-bipyridine)ruthenium(II) hexafluorophosphate at 1 μmol/L concentration. This dye has a decay constant of about 600 ns at room temperature (Van Houten and Watts 1976). This ensures fluorescence will be significant throughout the duration that the excited dye is in the observation volume. The objective lens chosen to create the confocal volume is a water-immersed Olympus *UPLSAPO 60XW* with a numerical aperture of 1.2. The detector is an ID100 Visible Single-Photon Detector from ID Quantique and is connected to a Becker-Hickl SPC-154 single photon counting TCSPC card allowing for data collection.

The concept behind the technique is shown in Fig. 2. A pulse from the excitation beam excites the dye in the confocal volume. Immediately after the pulse, only excited dye remains in the confocal volume and is fluorescing. As the fluorescing dye leaves the confocal volume due to the speed of the fluid, the intensity of the fluorescence decreases. The rate at which the fluorescence intensity decreases contains information about the fluid speed in the observed confocal volume. The only source of illumination in the channel is the laser light exiting the objective. The objective is overfilled ensuring the confocal spot created is very nearly diffraction limited. The pinhole is selected to be 50 μm which is approximately 1 airy disk in diameter. This pinhole does the depth-of-field selection ensuring only the confocal volume spot is selected such that only signal found in the confocal plane is sent to the detectors and prevents out of plane light from entering the detectors. One airy disk is the practical solution described in some papers (Park et al. 2004; Cox and Sheppard 2004) to ensure high resolution in depth, and enough signal-to-noise ratio. A diffraction-limited spot provides the smallest possible lateral dimension for the confocal

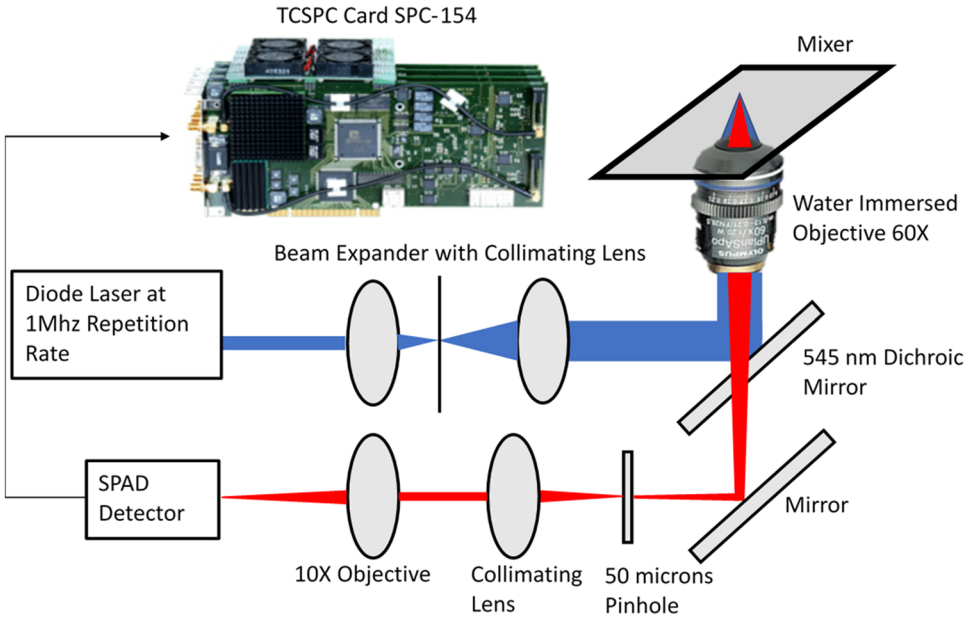

Fig. 1 Schematic of confocal fluorescence microscope setup used for velocimetry studies

volume without using super resolution techniques (Schermelleh et al. 2010). The open question on this technique which we are not able to provide more insight is that there will be excited solution entering the observation volume from above and below the confocal volume (selected via the pinhole) affecting the resultant decay due to velocity, but to what extent would require further study. We believe this issue can be resolved by using a two-photon microscopy setup instead of a confocal microscopy setup.

To collect data for a cross-section of a channel, scanning of multiple points in a grid-like manner is required. In this study, grid points spaced 3 µm by 3 µm apart per cross-section is selected. Figure 3 shows the geometry of the microfluidic protein mixer used in this study along with the locations of the cross-sections (slices) used for calibration of the system (calibration slice) and measurements of the speed (slices 1 and 2). All results are presented in the planes shown in Fig. 3.

2.1 Processing collected raw data

The first integral moment ω (ns) of the curve (Bostock et al. 1982) is used to characterize the decay at each grid point, the decays are shown in more detail in Sect. 2.3. Equation (1) is used for calculating the first moment ω where $T = 1000$ ns.

$$\omega = \sum(\text{Photon Counts}_i)t_i / \sum(\text{Photon Counts}_i) \approx \int_0^T p(t)t\mathrm{d}t / \int_0^T p(t)\mathrm{d}t. \quad (1)$$

Multiple decays collected over a span of 2 s, giving a time-averaged ω, per point is used for all measurements using Eq. (1). If an exponential decay, $p(t) = Ae^{-\lambda t}$, is assumed, then the first moment is related to the decay rate via $\omega = \frac{1}{\lambda} + \frac{T}{1-e^{\lambda T}}$. In this study, the time t where a measurement occurs at is determined from the period between pulses of the laser which is 1000 ns (1 MHz repetition rate). Having determined the first moment, ω, of the decay data collected at each grid point in the calibration slice, this is related to fluid speed via a calibration of the system where the velocity is known. The dimensions of the calibration slice are 30 µm wide by 100 µm deep. The raw data showing the decays is given in Sect. 2.2.

2.2 Calibration study on curve fitting ω with speed

To relate via curve fitting, ω and speed, Poiseuille flow (Nguyen 2011) with three different average speeds of 5000 mm/s, 6000 mm/s and 7000 mm/s were tested in the channel at the calibration slice. The Reynolds numbers at these speeds in the calibration slice is around a 100 making the flow laminar. Figure 4 shows ω (the first moment of decay) for all 3 test cases.

It should be noted that the white space in figures depicting ω is the region where the system cannot measure because the confocal volume is too close to the wall. This technique relies on excited dye leaving the confocal volume. The dye must leave the confocal volume before the next laser pulse arrives. Hence, where flow is slow (near the walls), the next laser pulse will arrive before all excited dye from

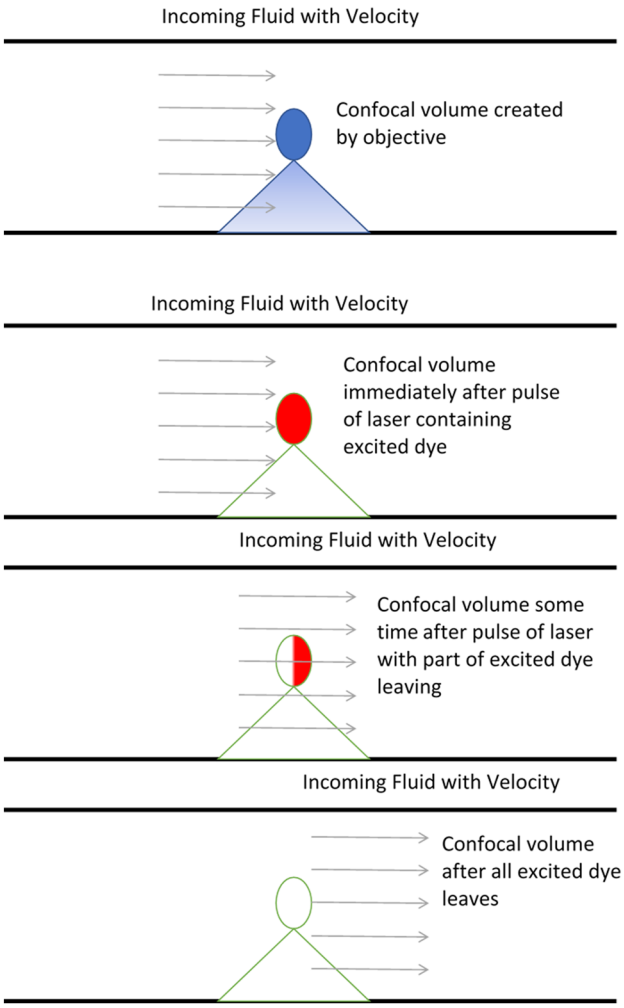

Fig. 2 Concept behind high-speed velocimetry using confocal fluorescence decay microscopy

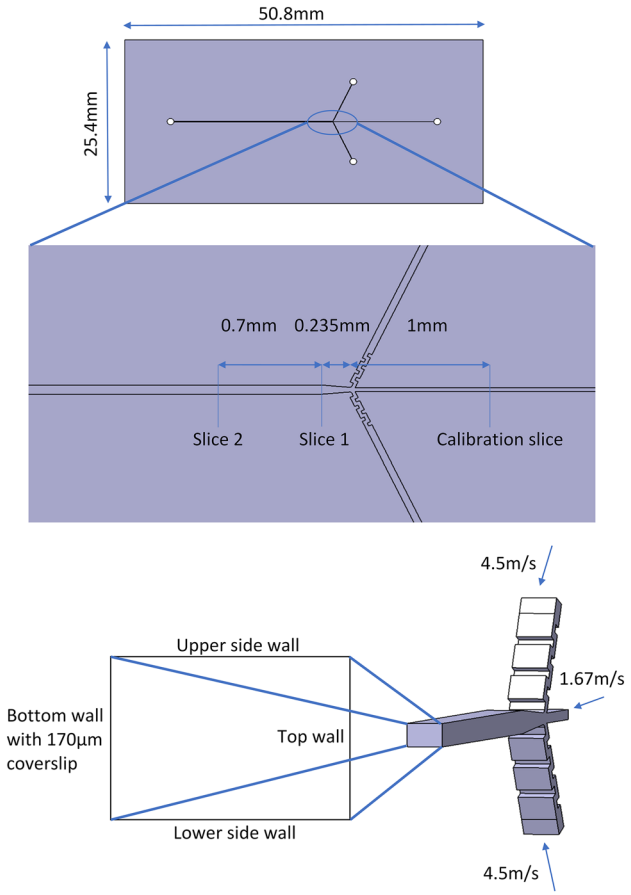

Fig. 3 Schematic of microfluidic mixer used and details pertaining to locations sampled and geometry, results are presented in the plane shown in the second image and at the locations shown in the first image. Flow is right to left in the first image and out of the page in the second image

the previous pulse leaves the confocal volume making processing the data near the walls significantly more difficult. Further study is required to determine wall speeds near wall using this technique. The lowest speed limit is discussed in the Sect. 4.

A tri-linear calibration function as shown in Eq. (2), where d is the channel depth and w is the channel width was constructed. The reason $1/\omega$ was selected is because $1/\omega$ is approximately the time constant of an exponential decay. This function is curve fitted to $1/\omega$, d and w with the theoretical Poiseuille flow at a particular average speed. The parameters from that curve fit are then used to determine speed from the other two average speed's data (ω) to determine how valid the parameters determined from a curve fit at one particular average speed can be used to predict speed from other average flow speeds' data (ω).

Theoretical Poiseuille flow speed

$$= a_1 + a_2 d + a_3 w + a_4 \frac{1}{\omega} + a_5 dw + a_6 w \frac{1}{\omega} + a_7 d \frac{1}{\omega} + a_8 dw \frac{1}{\omega}. \quad (2)$$

The constants of this function curve fitting speed to ω are determined by a least-squares fit (Acton 1959). Table 1 shows the constants of the curve fits for all three test cases.

From Table 1, it can be seen that most parameters are in similar ranges. The parameter that differs the most is a_6 which is the parameter of the nonlinear term with width and $1/\omega$. It can be seen from Fig. 4 that the gradient across the width towards the top wall becomes non-trivial and somewhat different for different average speeds. It is hypothesized that this is due to a slight angle of the laser with the vertical. In each test case, this alignment of the laser with the vertical was slightly different.

Once the constants for each test case are determined, the error in the curve fit was determined using the root mean

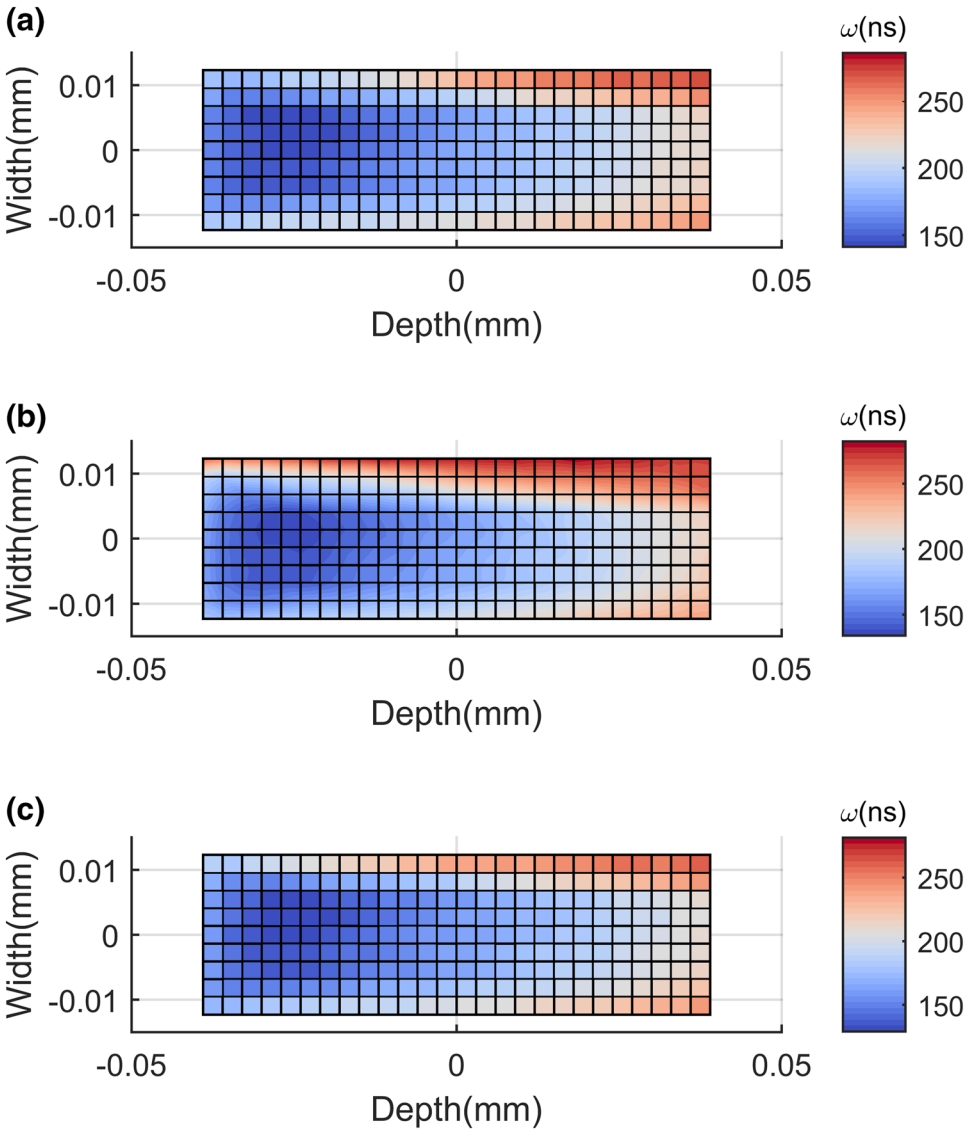

Fig. 4 ω computed from decays using the diode laser for Poiseuille flow. **a** 5000 mm/s, **b** 6000 mm/s, **c** 7000 mm/s

Table 1 Tri-linear curve-fit parameters determined at 5000 mm/s, 6000 mm/s and 7000 mm/s using diode laser from theoretical Poiseuille flow solutions at those respective speeds

Speed (mm/s)	$a_1 \times 10^4$	$a_2 \times 10^5$	$a_3 \times 10^6$	$a_4 \times 10^7$	$a_5 \times 10^5$	$a_6 \times 10^6$	$a_7 \times 10^6$	$a_8 \times 10^8$
5000	− 1.129	− 1.543	3.522	4.895	2.029	− 13.47	− 4.648	11.15
6000	− 1.117	− 1.519	3.638	4.845	1.206	12.17	− 5.041	12.52
7000	− 1.260	− 1.752	4.043	5.472	2.241	− 4.938	− 4.478	9.703

square error where deviations of the curve fit from the theoretical speed are used. Furthermore, constants from the 5000 mm/s curve fit were used to predict speed from 6000 and 7000 mm/s data and the error determined using the root mean square of deviations of the curve fit from the theoretical speed. The same was done for parameters from the 6000 mm/s parameters applied to 5000 mm/s and 7000 mm/s data, and for parameters from the 7000 mm/s parameters applied to 5000 mm/s and 6000 mm/s data. These results are shown in Table 2.

From Table 2, the curve-fitting parameters work best for their own data. This is to be expected. But, the calibration constants from one test also match other test cases with reasonable accuracy. It is interesting to note that it appears advantageous to do calibrations of this system at higher speeds. The higher average speed constants provide the least error for the

Table 2 Root mean square error of calibration

	5000 mm/s curve fit (%)	6000 mm/s curve fit (%)	7000 mm/s curve fit (%)
5000 mm/s data	12.34	15.43	19.16
6000 mm/s data	20.38	14.73	13.57
7000 mm/s data	29.50	19.98	12.90

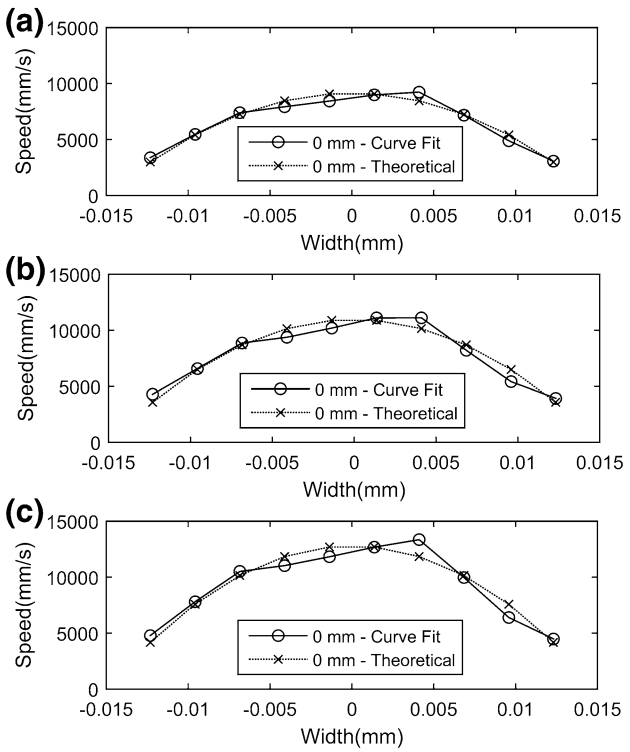

Fig. 5 Speed determined by curve fit compared to theoretical Poiseuille flow at 0 mm depth. **a** 5000 mm/s, **b** 6000 mm/s, **c** 7000 mm/s

other cases. We anticipate that with optimization of the system, errors of less than 5% could eventually be obtained.

Figure 5 shows the speed computed via the curve-fitting routine compared with the theoretical Poiseuille flow solution at a depth of 0 mm. As seen, the curve-fitted speed mostly tracks the Poiseuille flow solution within the root mean square error range. Again, with better optimization of the experiment, we anticipate it is possible to obtain curve fits that closely track the Poiseuille flow profile.

2.3 Further study into raw data and confocal volume geometry dependence

The flow profile in Fig. 4c where the average speed is 7000 mm/s is studied further. Figure 6 shows decays where the flow is present and the decays where no flow is present is for three grid points starting from the upper side wall and ending at the center of the channel at depths of −0.04 mm and 0.0105 mm are presented. The three grid points shown are the first, second and fifth points starting from the upper side wall. From Fig. 6, the difference between flowing decays and no flow decays is clearly obvious. As seen for the flowing decays, grid points closer to the upper side wall have decays that are higher up on the plot resulting in larger first moments and decays closer to the center of the channel are lower in the plot resulting in smaller first moments. This is to be expected. However, when comparing the decays for both flow and no flow at depths of − 0.04 mm (Fig. 6a) and 0.0105 mm (Fig. 6b), the decays appear to have lower initial amplitude the further in depth the grid point is.

The decrease in decay amplitude as the further in depth the grid point scanned is can be explained by determining how the confocal volume behaves with depth. Fluorescence correlation spectroscopy (FCS) was performed at depths ranging from −0.04 to 0.04 mm at 0.01 mm increments using 1 nmol/L of Alexa 488 in the mixer. The amplitude, G_0, of the FCS curves provides the number of molecules, $\langle N \rangle$, in the confocal volume in a direct manner given by Eq. (3) (Buschmann et al. 2009), which is an indicator of the volume of the confocal volume. Because the objective is overfilled using the beam expander, the spot making up the confocal volume is diffraction limited. Equation (4) (Cox and Sheppard 2004) shows the relation for determining the diffraction-limited beam waist (width of the confocal volume) where λ is the wavelength of the laser and NA is the numerical aperture of the objective. Figure 7 shows the number of particles, $\langle N \rangle$, vs. depth which indicates how the confocal volume changes its volume with depth.

$$\langle N \rangle = \frac{1}{G_0}, \ \langle N \rangle > 1 \tag{3}$$

$$\text{Diffraction Limited Beam Waist Diameter} = \frac{1.22\lambda}{1.31\text{NA}}. \tag{4}$$

The relation in Eq. (4) usually gives the diffraction-limited beam waist diameter of the confocal volume found at depths just above the coverslip (−0.04 mm depth in this mixer) which is calculated to be 0.35 μm (lateral dimension). However, from Fig. 7, it can be seen that the confocal volume also increases in volume with depth, up to 8 times increase in volume from the bottom wall to the top wall. On approximation, this means that the lateral dimension of the confocal volume would increase twofold from the bottom wall of the mixer to the top wall of the mixer. This change in dimensions of the confocal volume explains the depthwise gradient seen in the processed ω in Fig. 4. The confocal volume is smaller at lower depths resulting in faster decays, hence smaller ω while being larger at higher depths results

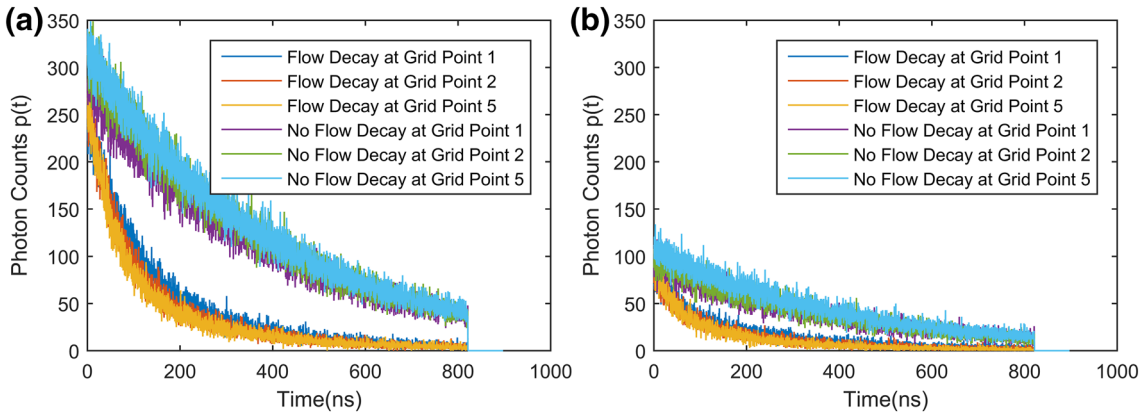

Fig. 6 Flow and no flow decays presented for grid points 1, 2 and 5 starting from the upper side wall of Fig. 4c. **a** −0.04 mm depth, **b** 0.0105 mm depth

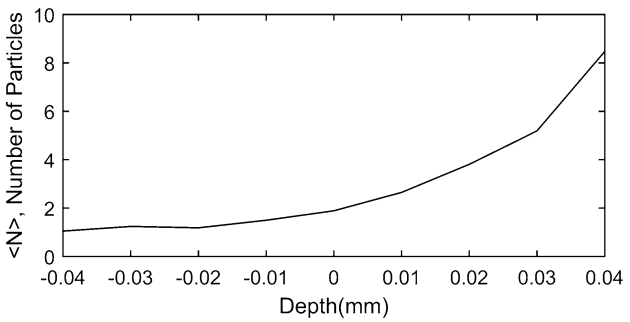

Fig. 7 Number of molecules in confocal volume with depth. The number of particles is a direct indicator of the volume of the confocal volume

in slower decays, hence it leads to larger ω. This change in confocal volume with depth also indicates that the confocal volume becomes larger and more diffuse (less intense) with increasing depth and would explain why the amplitude of the decays are decreasing with increasing depth. This is the reason why the functional form of the curve fit in Eq. (2) contains the depth, d, and first moment, ω. Width, w, is also present in the curve fit due to the mixer moving slightly during data collection and being at a slight angle with objective. Better vibration control in the setup and more robust clamping of the mixer is required to remove the width dependence.

Figure 8 shows ω at depths of −0.03 mm and 0 mm for Fig. 4. The standard deviation from five readings is also displayed in Fig. 8. As seen, the higher speeds due to increased flow rate causes the curves to drop indicating that the instrument is sensitive to change in speed and that first moments, ω, is a good way to characterize decays due to velocity.

3 Application of technique to a mixing problem

Significant study was undertaken to understand Poiseuille flows at the calibration slice using a pulsed diode laser. To demonstrate that the technique can be applied to different

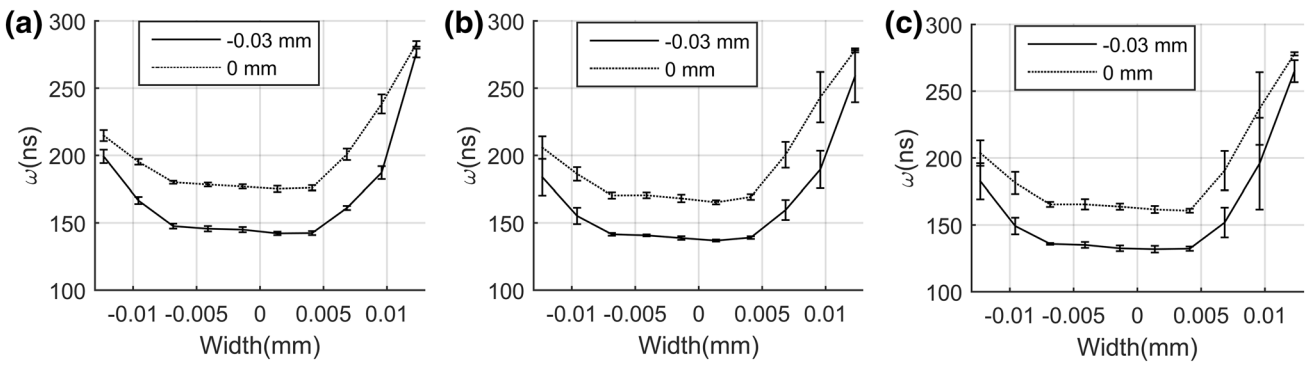

Fig. 8 ω at depths of −0.03 mm and 0 mm. **a** Fig. 4a: 5000 mm/s, **b** Fig. 4b: 6000 mm/s, **c** Fig. 4c: 7000 mm/s

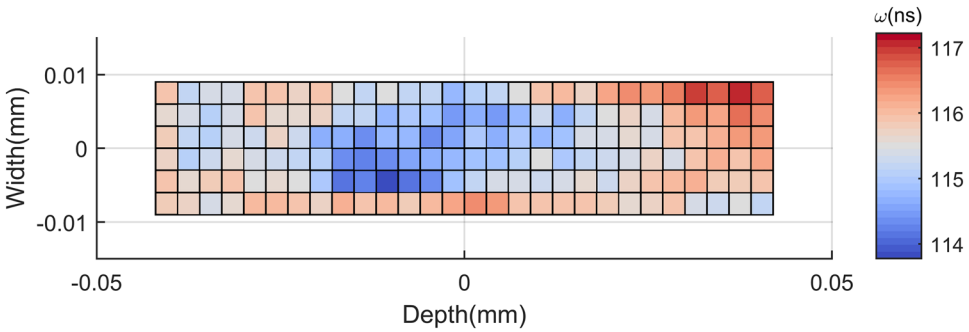

Fig. 9 ω collected using a Ti-Sapphire laser at 260 ns period between pulses (3.8 MHz repetition rate) with an average speed of 7000 mm/s at the calibration slice

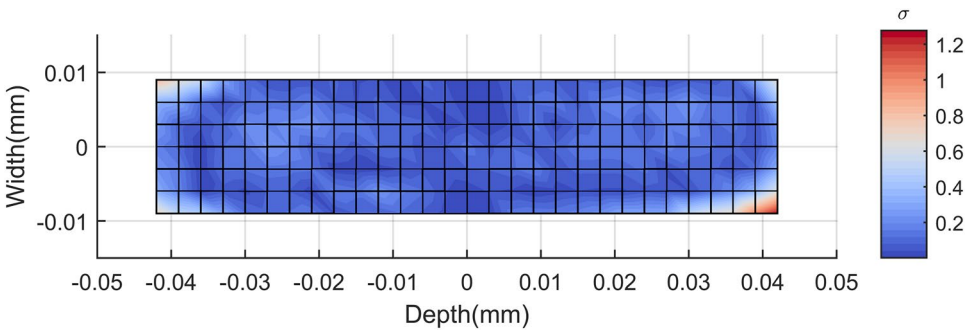

Fig. 10 Error of theoretical Poiseuille flow to curve-fitted speed function in Eq. (5) at 7000 mm/s using a Ti-Sapphire laser. Most of the error is at the top and bottom wall

confocal microscope setups, a 3.8 MHz repetition rate Ti-Sapphire laser is used in lieu of the 1 MHz diode laser. The geometry presented in Fig. 3 is a micro-mixer. It is desired to determine the velocity profile at slice 1 and slice 2 as shown in Fig. 3 to better understand the physics behind mixing.

Figure 9 shows the data collected at the calibration slice for an average speed of 7000 mm/s. The same curve-fitting routine is used as in Sect. 2.2, but with a bi-linear function instead of a tri-linear function. The reason for using a bi-linear function without the width, w, in the function is to allow the curve-fit parameters, determined at the calibration slice which is 30 µm wide, to be used to determine velocity at slice 1 and slice 2 which are 70 µm wide. This function is shown in Eq. (5), where d is depth.

$$\text{Theoretical Poiseuille flow speed} = b_1 + b_2 d + b_3 \frac{1}{\omega} + b_4 d \frac{1}{\omega}. \tag{5}$$

From Fig. 9, it is apparent that the Ti-Sapphire laser data is noisier than the data from the diode laser seen in Fig. 4 but there is less gradient present in both the width and depth. The root mean square error when calibrating against the theoretical Poiseuille flow at an average speed of 7000 mm/s is 22.75% and the error comparing the theoretical Poiseuille flow to the speed obtained from the curve fit given by Eq. (5) is shown in Fig. 10. Figure 11 shows the velocity determined from the curve fit compared to the theoretical Poiseuille flow solution at a depth of 0 mm. The velocity determined from the curve

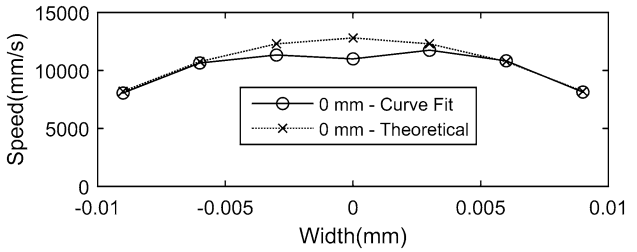

Fig. 11 Speed determined by curve fit compared to theoretical Poiseuille flow at 0 mm depth

fit mostly tracks the theoretical Poiseuille flow solution within the root mean square error range. Table 3 shows the constants determined from the curve fit of the theoretical Poiseuille flow solution to the raw data, ω and d, in Fig. 9.

3.1 Application of curve-fitted parameters to determine speed at slice 1 and slice 2

Now that a curve fit relates ω, d and speed, it is possible to use the parameters determined in Table 3 to determine the speed at slice 1 and slice 2 using Eq. (6). The assumption is that curve-fit parameters in Table 3 determined at the calibration slice are valid at slice 1 and slice 2. The cross-section at slice 1 and 2 is 70 µm wide by 100 µm deep. Figure 12 shows ω measured at slice 1 and slice 2.

Table 3 Bi-linear curve-fit parameters determined at 7000 mm/s using the Ti-Sapphire laser from theoretical Poiseuille flow solution

Speed (mm/s)	$b_1 \times 10^5$	$b_2 \times 10^5$	$b_3 \times 10^7$	$b_4 \times 10^8$
7000	−2.290	−9.045	2.760	1.072

$$\text{Speed} = -2.290 \times 10^5 - 9.045 \times 10^5 d + 2.760 \times 10^7 \frac{1}{\omega} + 1.072 \times 10^8 d \frac{1}{\omega}. \quad (6)$$

Using Eq. (6), the speed at slice 1 and slice 2 can be determined. Figure 13 shows the speed determined at slice 1 and slice 2. In slice 1, the flow has its highest speed towards the bottom wall of the mixer, while in slice 2, the peak moves towards the lower side wall. This indicates some bulk rotation in the flow after all three channels meet and mixing starts. The results also show the flow is sticking to the bottom wall of the mixer. To determine the precision of the setup, four repeats were taken and the standard deviation from the mean ω calculated. Using a propagation of error formula (Ku 1966) to relate the standard deviation of ω to speed, the speed with standard deviations for slice 1 and slice 2 at −0.03 mm and 0 mm depths are shown in Fig. 14. The formula is given in Eq. (7).

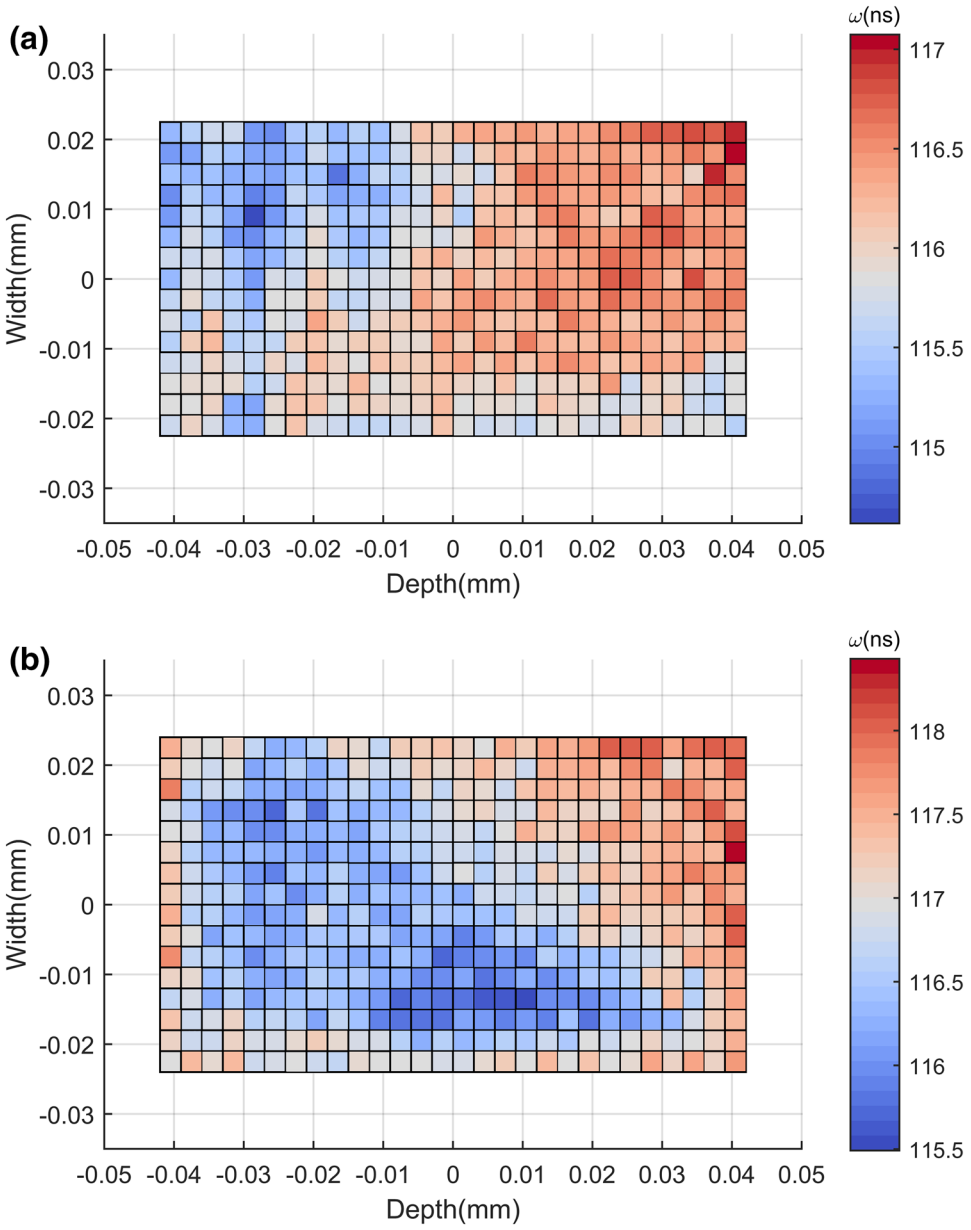

Fig. 12 ω collected at slice 1 and slice 2. Note that pulse rate is 260 ns, hence ω is lower than that of the diode laser ω. **a** Slice 1, **b** slice 2

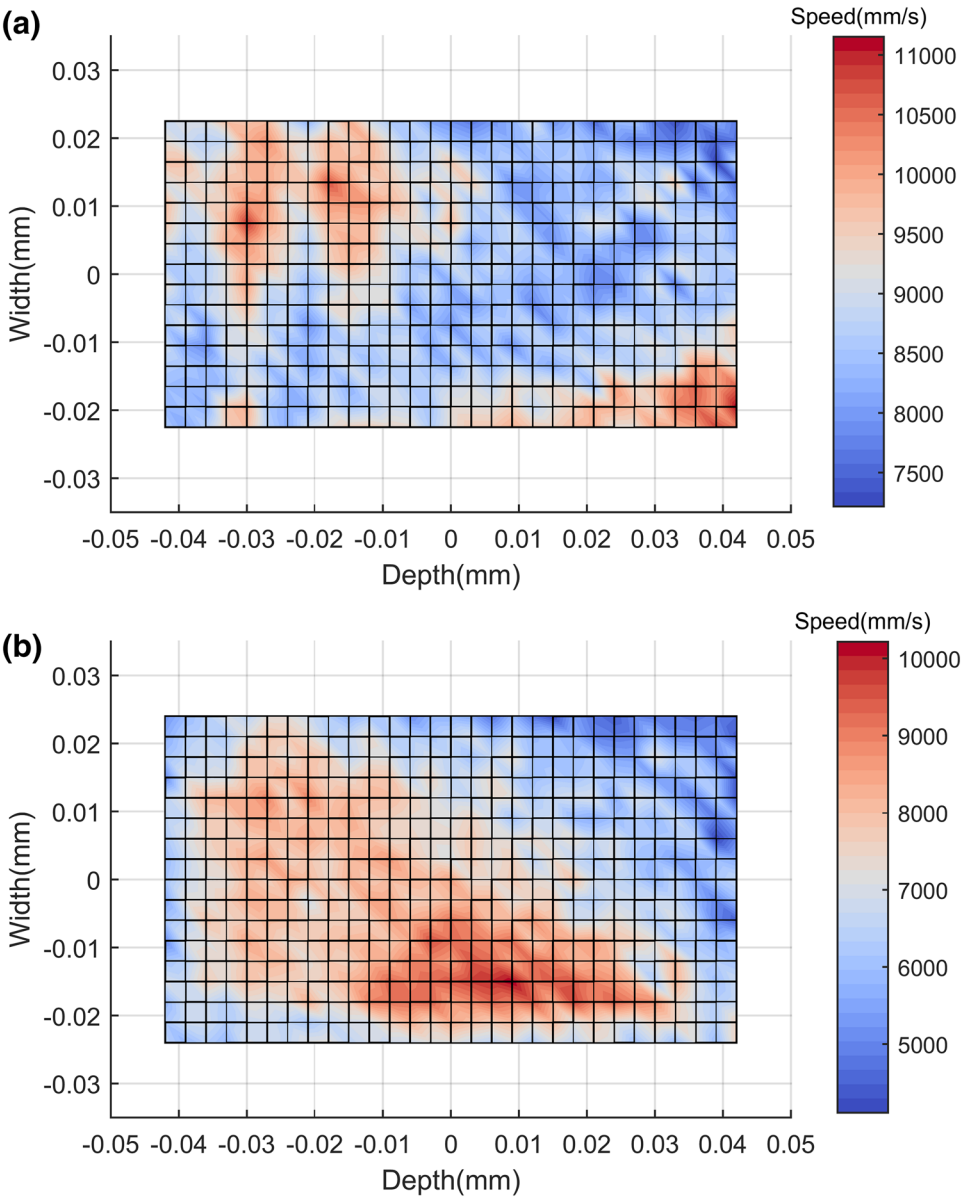

Fig. 13 Speed determined at slice 1 and slice 2. **a** Slice 1, **b** slice 2

$$\sigma_{S,\omega} = \sqrt{\left(\frac{\partial S}{\partial \omega}\right)^2 \sigma_\omega^2}. \tag{7}$$

In Sect. 5, these experimental results are qualitatively compared to computational results to confirm the chaotic/marginally turbulent flow that the experiments indicate is occurring at slice 1 and slice 2. The computational results follow the computational approach of Martell et al. (2010) and Inguva et al. (2018).

4 Discussion

Some limitations exist for this technique. The first limitation involves the repetition rate of the laser and the size of the confocal volume which limit the ability to measure slower speeds. The second limitation involves the mode quality of the laser which affects the formation of the confocal volume and thereby the choice of the curve-fitting function.

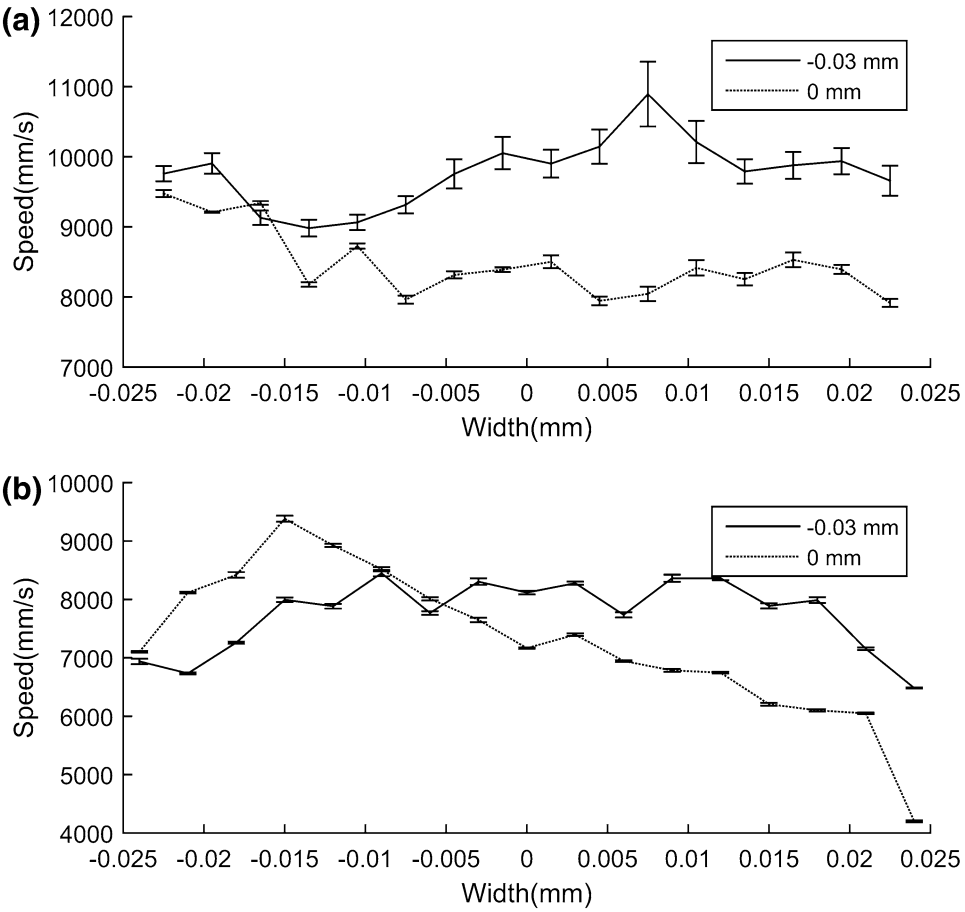

Fig. 14 Speed at **a** slice 1 and **b** slice 2 at −0.03 mm and 0 mm depths showing error bars

4.1 Confocal volume size and repetition rate

The lateral diameter of the confocal volume is between 0.35 and 0.70 µm depending on depth. Using the lateral diameter and the period between pulses of the laser, the theoretical lower limit of the measurable speeds can be determined. The direction of the flow is in the lateral dimension of the confocal volume. Using the formula for the lower limit speed in Eq. (8), the lower limit of the system is about 0.7 m/s for the diode laser and 2.7 m/s for the Ti-sapphire laser assuming the largest lateral dimension of the confocal volume at the top wall which is 70 µm. At speeds lower than 0.7 m/s for the diode laser and 2.7 m/s for the Ti-sapphire laser, the next laser pulse will arrive before all the excited dye leaves the confocal volume. This would result in decay events that contain information about two or more pulses rendering the decay data collected more difficult to post-process. In principle, with slower repetition rates, slower speeds near the wall can also be determined. However, if the repetition rate is too slow, the collected decay event will also contain information about the dye's excitation decay rate.

$$\text{Lower Limit Speed} = \frac{\text{Largest Lateral Diameter of Confocal Volume (microns)}}{\text{Period between Pulses (ns)}}. \quad (8)$$

Because the technique relies on the decay of fluorescence through the confocal volume, it can only provide information about the bulk flow speed and cannot give vector quantities at each grid point. Furthermore, the decay is collected as an average over numerous pulse periods spanning a total time interval of 2 s to ensure a high enough signal-to-noise ratio meaning the technique can only give the 2 s time-averaged speed at each grid point.

4.2 Mode quality of laser

The Ti-sapphire laser required the use of a doubling crystal to achieve the necessary wavelength to excite the dye which resulted in a reduced mode quality. The diode laser outputs the necessary wavelength with a perfectly round mode quality. Figure 15 shows the difference in mode quality between the Ti-sapphire laser and diode laser. FCS, in Fig. 7, showed that for the diode laser, the confocal volume's volume increases eightfold from the bottom wall to the top wall. This would explain the depthwise gradient seen in

Fig. 15 Mode quality comparison between Ti-sapphire laser and diode laser

Fig. 4 and explains why the smallest ω is not at the center of the channel but towards to the bottom.

The Ti-sapphire laser also has a slighter depthwise gradient with the lowest ω being closer to the bottom wall than at the center. An FCS study was not done with the Ti-Sapphire because we were not confident we could attain FCS curves given the poor mode quality of the Ti-Sapphire laser.

It is inferred that due to the poor mode quality of the Ti-sapphire, the confocal volume formed is irregular and diffuse at the bottom of the mixer and is therefore not subject to the significant volume change with depth that the diode laser confocal volume is experiencing. This diffused volume might also be the reason why there is less gradient widthwise for the Ti-Sapphire laser compared to the diose laser. However, it is acknowledged that further study into the confocal volume created by the Ti-sapphire laser is required to be certain. Furthermore, it could also be possible that collecting decay events over 1000 ns (for the diode laser) instead of 260 ns (for the Ti-Sapphire laser) cause the variation with depth.

5 Comparison of experimental results with computational simulations

A direct numerical simulation (DNS) of the Navier–Stokes equations was performed (Zusi and Perot 2013). To meet the requirements of a DNS, all time scales and turbulence scales must be resolved (Perot 2011). The time scale and smallest scale of turbulence (Kolmogorov scale) is given (Pope 2001a, b) by Eqs. (9) and (10), respectively:

$$\tau_\eta = \left(\frac{\nu}{\varepsilon}\right)^{1/2} \tag{9}$$

$$\eta = \left(\frac{\nu^3}{\varepsilon}\right)^{1/4}. \tag{10}$$

In addition, near a wall, the turbulence scales with the nondimensional distance to the wall using y^+ (Pope 2001a, b) and the DNS criteria of Jiang and Lai (2016). The definition is shown in Eq. (11). Using y^+, the distance of the fist gird point above the wall is determined and that distance is propagated for all following grid points until the center of the channel. To ensure the time scale is resolved properly, the criteria for the Courant number (Courant et al. 1967) of the simulation is shown in Eq. (12):

$$y^+ = \frac{y}{\nu}\sqrt{\nu\left(\frac{\partial\langle U\rangle}{\partial y}\right)_{\text{Wall}}} < 1 \tag{11}$$

$$Co = \frac{U_x\Delta t}{\Delta x} + \frac{U_y\Delta t}{\Delta y} + \frac{U_z\Delta t}{\Delta z} < 1. \tag{12}$$

The experiment was carried out using two pumps to drive fluid through the protein mixer. The first pump supplied the two side inlets while the second pump supplied the center inlet. To determine the cause of the flow sticking to bottom side wall, two DNS simulations were carried out. The first DNS simulation has the side inlets with flow at the same speed of 4.5 m/s, while the second DNS simulation has one side inlet at 5% higher speed of 4.725 m/s and the second side inlet at 5% lower speed of 4.375 m/s. This was done as the side inlets may have different flow rates due to being fed by a single pump which enforces equal pressure but not necessarily equal flow rate. Furthermore, to determine the ensemble average from the DNS simulations, temporal averaging was performed to create the ensemble average from simulations so as to compare directly to experimental results which are also time averages.

Figure 16 shows the DNS results at slice 1 and 2 for symmetric side inlet speeds of 4.5 m/s and Fig. 17 shows the DNS results at slice 1 and 2 for asymmetric side inlet speeds ± 5% from 4.5 m/s. Figure 18 shows streamlines inside the

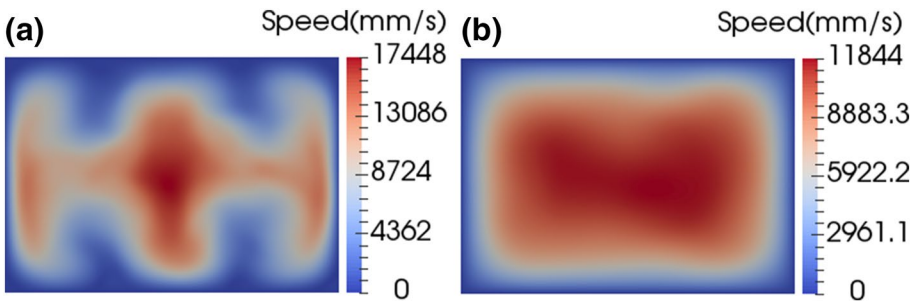

Fig. 16 Average speed with symmetric side inlet speeds. **a** Slice 1, **b** slice 2

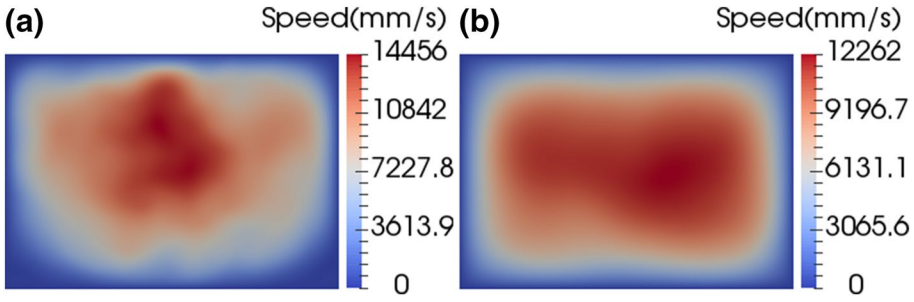

Fig. 17 Average speed with asymmetric ± 5% side inlet flow rates. **a** Slice 1, **b** slice 2

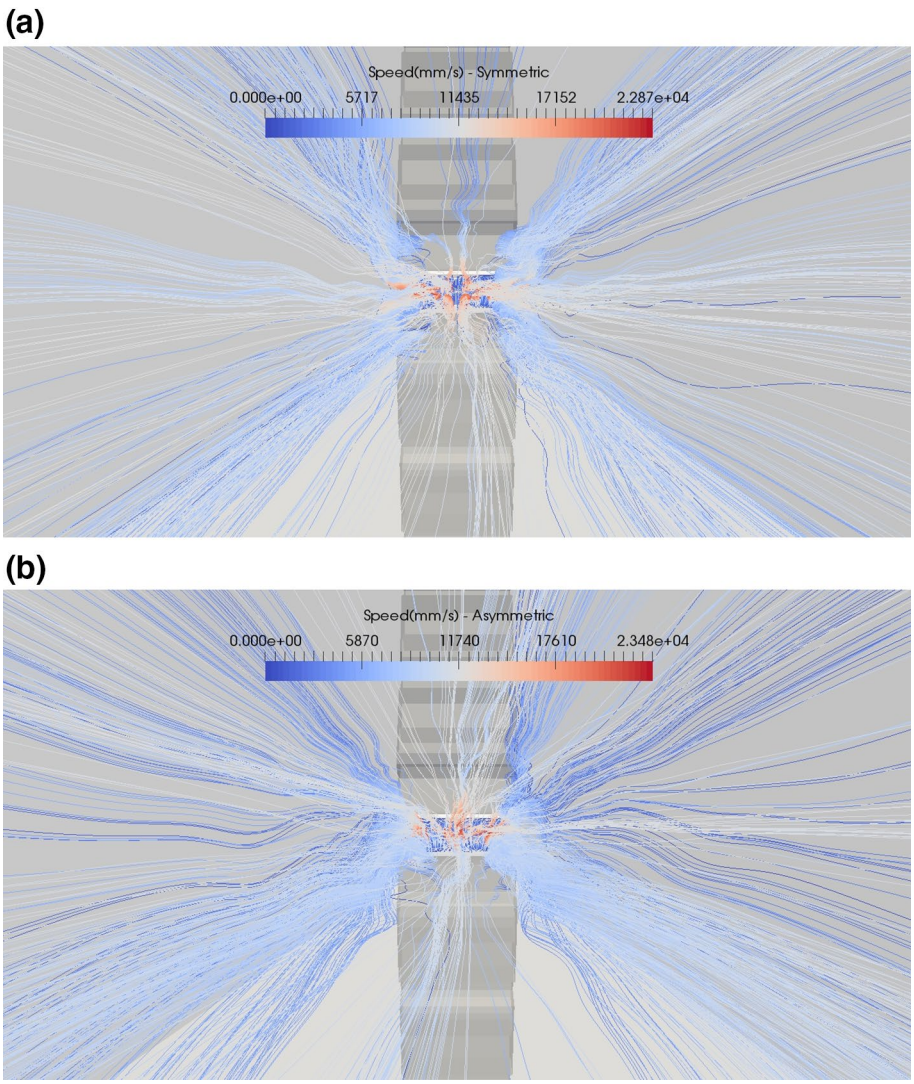

Fig. 18 Streamlines of speed in mixer for **a** symmetric side inlet flow rates, **b** asymmetric ± 5% side inlet flow rates

mixer for symmetric side inlet speeds and asymmetric side inlet speeds. From Fig. 18, it is seen that the asymmetric side inlets speeds do not create the speed profiles seen experimentally. The stream lines in Fig. 18 do not show any preference for the flow to the bottom wall like the experimental results do.

From the manufacturing of the chip, the bottom wall is smooth as a 170 µm cover slip was thermally fused to bottom. The top layer which consists of the top wall, upper side wall and lower side wall are etched and have a 2 µm peak to trove surface roughness profile due to the etching process to create the channel. As such, it can be hypothesized that at these flow rates where the Reynolds number based on half channel

width is 245 indicating transitional turbulence regime, that the flow jet might show an affinity for the smoother wall during mixing due to less drag on that surface.

6 Conclusion

A novel measurement technique has been developed that can, in theory, measure speeds upwards of 1,000,000 mm/s. In this paper, its use was demonstrated at speeds up to 10,000 mm/s. Two different lasers were used to demonstrate that the technique can be applied to different confocal microscope setups. The technique was applied to a high-speed micro-mixer to better understand the physics behind the mixing of the marginally chaotic device. The experimental setup demonstrated roughly a 20% error when measuring speeds. It is expected that with better vibration control, longer sampling periods, or alternative florescence molecules, those errors could potentially be reduced to 5%.

For future work, repetition rates of the laser and dye molecule choice must be investigated to determine the most optimal operating condition for the laser and the decay constant of the dye molecule such that first moments are not noisy and closely represent the paraboloid flow during calibration with a theoretical Poiseuille flow solution. It is also possible that using a two-photon confocal microscopy setup would allow speeds to be determined directly from decay events by characterizing the size of the two-photon confocal volume.

Direct numerical simulations which assumed all the walls were smooth suggest that asymmetric side inlet speeds partially confirm the experimental results. However, the computations do not fully explain the flow profiles seen from experimental results. Based on experimental results, the flow showed an affinity for the smooth bottom wall of the mixer during mixing.

Acknowledgements We would like to thank NSF for funding this work. The work is supported by NSF IDBR Award no. 1353942. We would like to thank Yvonne Chan at University of Massachusetts Medical School for providing assistance in the wet laboratory. We would like to thank the reviewers for their constructive feedback that significantly improved this paper. We acknowledge the Texas Advanced Computing Center (TACC) at The University of Texas at Austin for providing HPC, visualization and database resources that have contributed to the research results reported within this paper. http://www.tacc.utexas.edu.

References

Acton FS (1959) Analysis of straight-line data. Wiley, New York

Bostock L, Chandler S, Rourke C (1982) Further pure mathematics. Nelson Thornes, Cheltenham, p 410

Buschmann V, Krämer B, Koberling F, Macdonald R, Rättinger S (2009) Quantitative FCS: determination of the confocal volume by FCS and bead scanning with the microtime 200. Application Note PicoQuant GmbH, Berlin

Courant R, Friedrichs K, Lewy H (1967) On the partial difference equations of mathematical physics. IBM J Res Dev 11:215–234

Cox G, Sheppard CJ (2004) Practical limits of resolution in confocal and non-linear microscopy. Microsc Res Tech 63:18–22

Gobby D, Angeli P, Gavriilidis A (2001) Mixing characteristics of T-type microfluidic mixers. J Micromech Microeng 11:126

Inguva V, Kathuria SV, Bilsel O, Perot BJ (2018) Computer design of microfluidic mixers for protein/RNA folding studies. PLoS One 13:e0198534

Jiang X, Lai C (2016) Numerical techniques for direct and large-eddy simulations. CRC Press, Boca Raton

Kathuria SV, Chan A, Graceffa R, Paul Nobrega R, Robert Matthews C, Irving TC, Perot B, Bilsel O (2013) Advances in turbulent mixing techniques to study microsecond protein folding reactions. Biopolymers 99:888–896

Kinoshita H, Kaneda S, Fujii T, Oshima M (2007) Three-dimensional measurement and visualization of internal flow of a moving droplet using confocal micro-PIV. Lab Chip 7:338–346

Ku HH (1966) Notes on the use of propagation of error formulas. J Res Natl Bur Stand 70:263–273

Li H, Olsen MG (2006) Examination of large-scale structures in turbulent microchannel flow. Exp Fluids 40:733–743

Majumdar ZK, Sutin JD, Clegg RM (2005) Microfabricated continuous-flow, turbulent, microsecond mixer. Rev Sci Instrum 76:125103

Martell MB, Rothstein JP, Perot JB (2010) An analysis of superhydrophobic turbulent drag reduction mechanisms using direct numerical simulation. Phys Fluids 22:065102

Matsumoto S, Yane A, Nakashima S, Hashida M, Fujita M, Goto Y, Takahashi S (2007) A rapid flow mixer with 11-μs mixing time microfabricated by a pulsed-laser ablation technique: observation of a barrier-limited collapse in cytochrome c folding. J Am Chem Soc 129:3840–3841

Natrajan V, Christensen K (2009) Structural characteristics of transition to turbulence in microscale capillaries. Phys Fluids 21:034104

Nguyen N (2011) Micromixers: fundamentals, design and fabrication. Elsevier, Oxford, pp 28–36

Park JS, Choi CK, Kihm KD (2004) Optically sliced micro-PIV using confocal laser scanning microscopy (CLSM). Exp Fluids 37:105–119

Perot JB (2011) Determination of the decay exponent in mechanically stirred isotropic turbulence. AIP Adv 1:022104

Pope SB (2001a) The scales of turbulent motion. In: Turbulent flows, pp 184–187

Pope SB (2001b) Wall flows. In: Turbulent flows, p 270

Schermelleh L, Heintzmann R, Leonhardt H (2010) A guide to super-resolution fluorescence microscopy. J Cell Biol 190:165–175. https://doi.org/10.1083/jcb.201002018

Shinohara K, Sugii Y, Aota A, Hibara A, Tokeshi M, Kitamori T, Okamoto K (2004) High-speed micro-PIV measurements of transient flow in microfluidic devices. Meas Sci Technol 15:1965

Tanaami T, Otsuki S, Tomosada N, Kosugi Y, Shimizu M, Ishida H (2002) High-speed 1-frame/ms scanning confocal microscope with a microlens and Nipkow disks. Appl Opt 41:4704–4708

Van Houten J, Watts RJ (1976) Temperature dependence of the photophysical and photochemical properties of the tris (2,2′-bipyridyl)ruthenium(II) ion in aqueous solution. J Am Chem Soc 98:4853–4858

Van Oort B, Amunts A, Borst JW, Van Hoek A, Nelson N, Van Amerongen H, Croce R (2008) Picosecond fluorescence of intact and dissolved PSI-LHCI crystals. Biophys J 95:5851–5861

Williams SJ, Park C, Wereley ST (2010) Advances and applications on microfluidic velocimetry techniques. Microfluid Nanofluidics 8:709–726

Zettner C, Yoda M (2003) Particle velocity field measurements in a near-wall flow using evanescent wave illumination. Exp Fluids 34:115–121

Zusi CJ, Perot JB (2013) Simulation and modeling of turbulence subjected to a period of uniform plane strain. Phys Fluids 25:110819

Affiliations

Venkatesh Inguva[1] · Jonathan P. Rothstein[1] · Osman Bilsel[2] · Blair J. Perot[1]

[1] University of Massachusetts Amherst, Amherst, MA 01003, USA

[2] University of Massachusetts Medical School, Worcester, MA 01655, USA